Fluid pressure diffusion effects on the excess compliance matrix of porous rocks containing aligned fractures

Gabriel A. Castromán [1], Nicolás D. Barbosa [2], J. Germán Rubino [3], Fabio I. Zyserman [1] and Klaus Holliger [4,5]

[1] *CONICET, Facultad de Ciencias Astronómicas y Geofísicas, Universidad Nacional de La Plata, La Plata, Argentina.*
E-mail: gcastroman@fcaglp.unlp.edu.ar
[2] *Department of Earth Sciences, University of Geneva, Switzerland*
[3] *CONICET, Centro Atómico Bariloche - CNEA, San Carlos de Bariloche, Argentina*
[4] *Applied and Environmental Geophysics Group, Institute of Earth Sciences, University of Lausanne, Lausanne, Switzerland*
[5] *School of Earth Sciences, Zhejiang University, Hangzhou, China*

SUMMARY

The presence of sets of open fractures is common in most reservoirs, and they exert important controls on the reservoir permeability as fractures act as preferential pathways for fluid flow. Therefore, the correct characterization of fracture sets in fluid-saturated rocks is of great practical importance. In this context, the inversion of fracture characteristics from seismic data is promising since their signatures are sensitive to a wide range of pertinent fracture parameters, such as density, orientation and fluid infill. The most commonly used inversion schemes are based on the classical linear slip theory (LST), in which the effects of the fractures are represented by a real-valued diagonal excess compliance matrix. To account for the effects of wave-induced fluid pressure diffusion (FPD) between fractures and their embedding background, several authors have shown that this matrix should be complex-valued and frequency-dependent. However, these approaches neglect the effects of FPD on the coupling between orthogonal deformations of the rock. With this motivation, we considered a fracture model based on a sequence of alternating poroelastic layers of finite thickness representing the background and the fractures, and derived analytical expressions for the corresponding excess compliance matrix. We evaluated this matrix for a wide range of background parameters to quantify the magnitude of its coefficients not accounted for by the classical LST and to determine how they are affected by FPD. We estimated the relative errors in the computation of anisotropic seismic velocity and attenuation associated with the LST approach. Our analysis showed that, in some cases, considering the simplified excess compliance matrix may lead to an incorrect representation of the anisotropic response of the probed fractured rock.

Key words: Fracture and flow; Numerical approximations and analysis; Acoustic properties; Wave propagation.

1 INTRODUCTION

The presence of fractures is a common characteristic throughout the Earth's upper crust. As fractures exert a strong influence on the mechanical and hydraulic properties of the affected rock masses, their identification and characterization is of great importance in fundamental and applied geophysics. In particular, open fractures tend to control the permeability of a reservoir as they may act as preferential pathways for fluid flow. At typical reservoir depths, these fractures tend to be oriented normal to the direction of minimum *in situ* stress (Schoenberg & Sayers 1995). Since this direction is generally horizontal, the presence of sets of aligned, subvertical fractures is rather common in most reservoirs (Liu *et al.* 2000). The seismic method is a valuable tool for the detection and characterization of fractures, due to the fact that seismic waves experience strong directional dependence, and are also significantly attenuated and delayed when propagating through fractures (Maultzsch *et al.* 2003). For this reason, there is currently great interest in improving the understanding of seismic wave propagation through fractured rocks in general, and in presence of subvertical fractures in particular (Foord *et al.* 2015; Xue *et al.* 2017). Since seismic methods usually lack the resolution needed to directly image individual fractures, most efforts in this direction focus on exploiting the information encoded in the effective seismic properties of the probed fractured material.

To extract the properties of a fractured system, such as predominant orientation, intensity and type of material infill from seismic data, it is necessary to relate these characteristics to the effective anisotropic seismic response of the probed medium. Arguably, the most common approach to achieve this is based on the linear slip theory (LST, Schoenberg 1980; Pyrak-Nolte *et al.* 1990). Therein, the fractures are treated as interfaces separating two solid materials representing the embedding background rock. Although the stresses remain continuous across such interfaces, the seismic effect of the fractures manifests itself as a discontinuity in the solid displacement field associated with the seismic wave propagation. In the framework of this theory, the seismic response of the fractured rock mass is expressed by means of its effective compliance matrix $\mathbf{S}$, which is the inverse of the effective stiffness matrix $\mathbf{C}$,

$$\mathbf{S} = \mathbf{S}^b + \delta\mathbf{S}, \tag{1}$$

where $\mathbf{S}^b$ is the compliance matrix of the background rock and $\delta\mathbf{S}$ is the excess compliance matrix due to the presence of the fractures (Schoenberg & Douma 1988). The advantage of this approach is that, for a single set of rotationally invariant vertical fractures perpendicular to the horizontal x_1-axis, the excess compliance matrix in the long-wavelength limit depends on only two parameters and, in Voigt notation, has a simplified structure of the form

$$\delta\mathbf{S}_{\text{LST}} = \begin{pmatrix} \eta_N & 0 & 0 & 0 & 0 & 0 \\ 0 & 0 & 0 & 0 & 0 & 0 \\ 0 & 0 & 0 & 0 & 0 & 0 \\ 0 & 0 & 0 & 0 & 0 & 0 \\ 0 & 0 & 0 & 0 & \eta_T & 0 \\ 0 & 0 & 0 & 0 & 0 & \eta_T \end{pmatrix}, \tag{2}$$

where η_N and η_T are the normal and tangential fracture compliances, respectively (Schoenberg & Sayers 1995). These compliances contain information regarding the internal structure or geometry of the fractures (Bakulin *et al.* 2000). When the background rock is assumed to be isotropic, the fractured reservoir effectively behaves as a horizontal transversely isotropic (HTI) medium.

In its original form, this framework was developed for elastic solids containing fractures and therefore the resulting elements of the effective compliance matrix are real-valued and frequency-independent (Schoenberg & Sayers 1995). However, when a seismic wave travels through a fluid-saturated porous rock containing fractures, local gradients in the pore fluid pressure arise due to the uneven mechanical response of the fractures and the embedding background rock. As a consequence, the pore fluid flows from the fractures into the background during the compressional cycle of the wave, and back to the fractures in the extensional cycle, a physical process known as wave-induced fluid pressure diffusion (FPD) or wave-induced fluid flow (Müller *et al.* 2010). This process is accompanied by energy loss due to viscous internal friction within the pore fluid and, consequently, produces attenuation and velocity dispersion of the seismic wave. Thus, to account for these effects in the modelling of the seismic response of a fractured medium, the components of the effective compliance matrix should be complex-valued and frequency-dependent (Krzikalla & Müller 2011). There exist different approaches to include FPD effects through the LST in the effective compliance matrix of a porous rock with aligned fractures. Most of them consist in replacing the elastic fracture compliances η_N and η_T with complex-valued and frequency-dependent parameters, while preserving the structure of the excess compliance matrix given by eq. (2) (Bakulin *et al.* 2000; Chichinina *et al.* 2006; Verdon *et al.* 2009; Rubino *et al.* 2015). Nevertheless, Gurevich (2003) showed that in the low-frequency limit, when fluid pressure equilibrium between fractures and the background rock is fully achieved, the associated excess compliance matrix has no longer the structure of eq. (2). Due to fluid pressure communication between fractures and background, a stress component parallel to the plane of the fractures influences the deformation of the fractured rock in a direction normal to this plane, and vice versa. This fact, in turn, implies that some other elements of the associated excess compliance matrix may be non-negligible and, hence, the use of eq. (2) may introduce errors in the computation of the anisotropic response of fluid-saturated rocks containing aligned fractures. Recently, Guo *et al.* (2018) proposed a model to compute the frequency-dependent effective anisotropic response of a fluid-saturated fractured porous medium using an excess compliance matrix with the simplified structure of eq. (2). The analytical procedure presented in their work was compared for a particular fractured rock sample with numerical upscaling simulations (Rubino *et al.* 2016) that provide a complete physical description of the corresponding medium. The results obtained show slight discrepancies in phase velocities and attenuation, which may be due to the use of the simplified structure of the excess compliance matrix in the model of Guo *et al.* (2018). To our knowledge, there is no systematic study on the magnitude and the dynamic behaviour of these additional excess compliances and their impact on the seismic response of fractured rocks.

Our aim in this work is, therefore, to provide a sensitivity analysis of these additional compliances for a wide range of poroelastic parameters of rocks containing a set of vertical fractures, and to evaluate the conditions under which they cannot be neglected. Moreover, we quantify the errors introduced in the calculation of the associated anisotropic seismic attenuation and phase velocities when the LST based on eq. (2) is used. This analysis serves as a guide for the quantification of the errors that may arise in the inversion of fracture parameters based on the commonly used LST from seismic data.

2 THEORY

Different approaches exist to compute the frequency-dependent effective stiffness matrix, or its inverse, the compliance matrix, of an isotropic fluid-saturated porous rock permeated by a set of aligned fractures (Chapman 2003; Brajanovski *et al.* 2005; Baird *et al.* 2013; Carcione
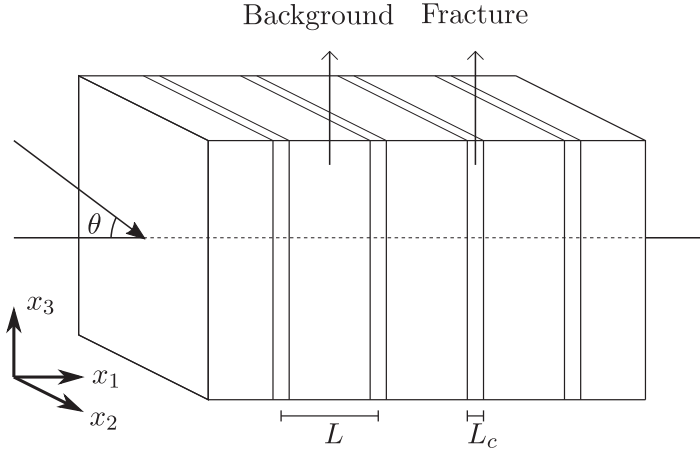
Figure 1. Geometry of the fracture system considered in this work. The angle of incidence θ is the angle between the x_1-axis of symmetry and the direction of wave propagation.

et al. 2013; Galvin & Gurevich 2015). They differ from each other with respect to the fracture geometry and distribution, and the physical phenomena associated with the seismic energy dissipation. For simplicity, we consider a set of regularly distributed parallel planar fractures of finite thickness and infinite lateral extent, similar to that used by Carcione *et al.* (2013). Therein, the elastic equivalent response of the probed medium at low and high frequencies is given by poroelastic Backus averaging. The effective dynamic response between these two frequency limits is controlled by FPD between fractures and the embedding background. In this section we give the geometrical details of the fracture system considered in this work and the expressions of the frequency-dependent elements of its effective stiffness matrix. Then, we provide explicit analytical expressions for the elements of the fracture excess compliance matrix.

2.1 Thin layer model

Following Brajanovski *et al.* (2005), we model a fluid-saturated porous rock mass with planar vertically aligned fractures as a regularly distributed system of relatively thick layers of isotropic porous background material alternating with very thin, highly porous and highly permeable layers representing the fractures (Fig. 1). The latter have a porosity ϕ_c, permeability κ_c, dry bulk modulus K_c^{dry}, shear modulus μ_c, and thickness, that is, aperture L_c. The distance between consecutive fractures is L and, thus, the thickness fraction of the fractures is $h_c = L_c/L$. The background material is characterized by a porosity ϕ_b, permeability κ_b, dry bulk modulus K_b^{dry}, shear modulus μ_b and its thickness fraction is $h_b = 1 - h_c$. We assume that, at the grain level, both background and fractures are composed of the same isotropic material, which has a bulk modulus K_g, shear modulus μ_g, and density ρ_g. The properties of the pore fluid in the background are the bulk modulus K_{fb}, density ρ_{fb}, and dynamic viscosity η_b. The fluid filling the fractures has a bulk modulus K_{fc}, density ρ_{fc}, and viscosity η_c. This representation of the fractured medium will be referred to as the thin layer model (TLM). In response to a passing seismic wave, this layered system behaves effectively as a homogeneous HTI medium when the predominant wavelengths are long compared to its characteristic length L. Moreover, its effective response will be frequency-dependent as it is affected by FPD between the fractures and their embedding background. The associated effective stiffness matrix is

$$\mathbf{C}(\omega) = \begin{pmatrix} C_{11}(\omega) & C_{12}(\omega) & C_{13}(\omega) & 0 & 0 & 0 \\ C_{12}(\omega) & C_{22}(\omega) & C_{23}(\omega) & 0 & 0 & 0 \\ C_{13}(\omega) & C_{23}(\omega) & C_{33}(\omega) & 0 & 0 & 0 \\ 0 & 0 & 0 & C_{44}(\omega) & 0 & 0 \\ 0 & 0 & 0 & 0 & C_{55}(\omega) & 0 \\ 0 & 0 & 0 & 0 & 0 & C_{66}(\omega) \end{pmatrix}, \tag{3}$$

where ω is the angular frequency. In the next subsections, we describe the behaviour of the TLM in the different frequency regimes.

2.1.1 Effective response of the TLM in the unrelaxed and relaxed states

For frequencies low enough to remain within the long-wavelength approximation, where scattering effects are negligible, but sufficiently high so that the fluid will have no time to flow between fractures and the host rock within a half-wave cycle, the fractures should be considered to be hydraulically isolated. That is, there is no pore fluid pressure communication between the fractures and the background, and the elastic properties of both fractures and background can be locally described by the isotropic Gassmann's equations (Gassmann 1951). This regime is called the 'unrelaxed' state (Müller *et al.* 2010). Backus (1962) derived explicit expressions for the five effective elastic parameters of such an equivalent TI medium. The coefficients of the associated stiffness matrix $\mathbf{C}^u$ are given in Appendix A. The corresponding effective compliance matrix $\mathbf{S}^u$ of the medium can be obtained by inverting the stiffness matrix $\mathbf{C}^u$.

For frequencies below the unrelaxed state and assuming that the fractures are hydraulically connected to the pore space of the background, there will be pore fluid pressure communication between these two regions in response to the propagation of a seismic wave. In the low-frequency limit, the pressure gradients induced by the large mechanical contrast between fractures and background have enough time to fully equilibrate and, hence, the pore fluid pressure is constant throughout the fractured rock. This frequency limit is called the 'relaxed' state (Müller *et al.* 2010). Gelinsky & Shapiro (1997) extended the result of Backus (1962) to fluid-saturated poroelastic layers for relaxed pore fluid pressure. The coefficients of the effective stiffness matrix in this case $\mathbf{C}^r$ are displayed in Appendix A. The effective compliance matrix in the relaxed case $\mathbf{S}^r$ can be obtained by inverting the stiffness matrix $\mathbf{C}^r$.

2.1.2 *Effective dynamic response of the TLM*

The stiffness matrices $\mathbf{C}^u$ and $\mathbf{C}^r$ describe the effective behaviour of the fractured system in the high- and low-frequency limits, respectively. There, neither attenuation nor dispersion take place, since, in both cases, the considered medium is elastic equivalent. At intermediate frequencies, though there is pore fluid pressure exchange between fractures and the background, fluid pressure equilibrium is only partially achieved. In this transitional frequency regime, energy dissipation due to FPD can take place, leading to frequency-dependent seismic attenuation and velocity dispersion (Müller *et al.* 2010). To account for these effects in the particular case of a regularly distributed 1-D medium with two alternating layers, White *et al.* (1975) derived an expression for the dynamic-equivalent *P*-wave modulus C_{11} as

$$\frac{1}{C_{11}(\omega)} = \frac{1}{C_{11}^u} + \frac{1}{(L/2)} \frac{(B_b - B_c)^2}{N_b k_b \coth(k_b h_b L/2) + N_c k_c \coth(k_c h_c L/2)}, \tag{4}$$

where $B = \alpha M/P^{\mathrm{sat}}$ is the uniaxial Skempton coefficient, that is, the ratio of the fluid pressure increase to the applied stress for undrained conditions, $N = M(1 - \alpha B)$, and $k = \sqrt{i\eta\omega/N\kappa}$ is the wavenumber of Biot's slow *P* wave. The poroelastic constants α and M as well as the undrained *P*-wave modulus P^{sat} are given in Appendix A. Eq. (4) allows to compute the properties of *P* waves propagating only in the direction normal to the plane of the layering. To generalize the FPD effects to either arbitrary angles of incidence or shear waves, Krzikalla & Müller (2011) proposed a methodology based on the fact that all the elements of the complete stiffness matrix have approximately the same fluid pressure relaxation behaviour. Therein, the coefficients of the effective stiffness matrix $\mathbf{C}(\omega)$ are given by

$$C_{ij}(\omega) = C_{ij}^u - R(\omega)\left[C_{ij}^u - C_{ij}^r\right], \tag{5}$$

where the effective elastic parameters at low- and high-frequency limits C_{ij}^r and C_{ij}^u, respectively, are linked by a single scalar function $R(\omega)$ that describes the frequency-dependent relaxation behaviour of the equivalent viscoelastic medium. This relaxation function can be computed by normalizing the dynamic-equivalent *P*-wave modulus at normal incidence $C_{11}(\omega)$ given by eq. (4) with its unrelaxed and relaxed limits,

$$R(\omega) = \frac{C_{11}(\omega) - C_{11}^u}{C_{11}^r - C_{11}^u}. \tag{6}$$

Once the relaxation function $R(\omega)$ is computed, we can completely define the effective stiffness matrix $\mathbf{C}(\omega)$ of the TLM using eq. (5) with its corresponding high- and low-frequency limits. This model describes the complete frequency-dependent seismic response of a fluid-saturated poroelastic medium with regularly distributed planar fractures of finite thickness. The frequency-dependent effective compliance matrix of the medium $\mathbf{S}(\omega)$ can be obtained by inverting the stiffness matrix $\mathbf{C}(\omega)$ for each frequency ω.

2.2 Fracture excess compliance matrix for the TLM

The effective compliance matrix of a fractured rock can be expressed as the sum of the compliance matrix of the unfractured background rock and the excess compliance matrix due to the presence of the fractures (Schoenberg & Douma 1988; Gurevich 2003). Due to the large compressibility contrast between the fractures and the background, the FPD effects on the mechanical response of the latter are rather negligible (Rubino *et al.* 2015). Correspondingly, the coefficients of the compliance matrix of the background $\mathbf{S}^b$ can be computed through standard isotropic Gassmann's equations as

$$S_{11}^b = S_{22}^b = S_{33}^b = \frac{\lambda_b^{\mathrm{sat}} + \mu_b}{\mu_b \left(3\lambda_b^{\mathrm{sat}} + 2\mu_b\right)}, \tag{7}$$

$$S_{12}^b = S_{13}^b = S_{23}^b = \frac{-\lambda_b^{\mathrm{sat}}}{2\mu_b \left(3\lambda_b^{\mathrm{sat}} + 2\mu_b\right)}, \tag{8}$$

$$S_{44}^b = S_{55}^b = S_{66}^b = \frac{1}{\mu_b}, \tag{9}$$

where λ_b^{sat} is the undrained Lamé parameter (Appendix A). Therefore, we obtain the fracture excess compliance matrix $\delta \mathbf{S}(\omega)$ for the TLM as

$$\delta \mathbf{S}(\omega) = \mathbf{S}(\omega) - \mathbf{S}^b = \begin{pmatrix} \delta S_{11}(\omega) & \delta S_{12}(\omega) & \delta S_{13}(\omega) & 0 & 0 & 0 \\ \delta S_{12}(\omega) & \delta S_{22}(\omega) & \delta S_{23}(\omega) & 0 & 0 & 0 \\ \delta S_{13}(\omega) & \delta S_{23}(\omega) & \delta S_{33}(\omega) & 0 & 0 & 0 \\ 0 & 0 & 0 & \delta S_{44}(\omega) & 0 & 0 \\ 0 & 0 & 0 & 0 & \delta S_{55}(\omega) & 0 \\ 0 & 0 & 0 & 0 & 0 & \delta S_{66}(\omega) \end{pmatrix}. \tag{10}$$

The explicit expressions for the coefficients of this matrix are given by

$$\delta S_{11}(\omega) = \frac{C_{22}(\omega) + C_{23}(\omega)}{D(\omega)} - \frac{\lambda_b^{\text{sat}} + \mu_b}{\mu_b \left(3\lambda_b^{\text{sat}} + 2\mu_b\right)}, \tag{11}$$

$$\delta S_{12}(\omega) = \frac{-C_{12}(\omega)}{D(\omega)} + \frac{\lambda_b^{\text{sat}}}{2\mu_b \left(3\lambda_b^{\text{sat}} + 2\mu_b\right)}, \tag{12}$$

$$\delta S_{13}(\omega) = \delta S_{12}(\omega), \tag{13}$$

$$\delta S_{22}(\omega) = \frac{C_{11}(\omega)C_{22}(\omega) - [C_{12}(\omega)]^2}{[C_{22}(\omega) - C_{23}(\omega)]\,D(\omega)} - \frac{\lambda_b^{\text{sat}} + \mu_b}{\mu_b \left(3\lambda_b^{\text{sat}} + 2\mu_b\right)}, \tag{14}$$

$$\delta S_{23}(\omega) = \frac{-C_{23}(\omega)C_{11}(\omega) + [C_{12}(\omega)]^2}{[C_{22}(\omega) - C_{23}(\omega)]\,D(\omega)} + \frac{\lambda_b^{\text{sat}}}{2\mu_b \left(3\lambda_b^{\text{sat}} + 2\mu_b\right)}, \tag{15}$$

$$\delta S_{33}(\omega) = \delta S_{22}(\omega), \tag{16}$$

$$\delta S_{44}(\omega) = \frac{1}{C_{44}(\omega)} - \frac{1}{\mu_b}, \tag{17}$$

$$\delta S_{55}(\omega) = \frac{1}{C_{55}(\omega)} - \frac{1}{\mu_b}, \tag{18}$$

$$\delta S_{66}(\omega) = \delta S_{55}(\omega); \tag{19}$$

with

$$D(\omega) = [C_{22}(\omega) + C_{23}(\omega)]\,C_{11}(\omega) - 2\,[C_{12}(\omega)]^2. \tag{20}$$

The set of eqs (11)–(20) is the main result of the theoretical derivation of this work. We obtain analytical expressions for all the elements of the fracture excess compliance matrix of the TLM. By comparing the structure of this matrix with that corresponding to the LST approach, which is given by eq. (2), we observe that some of its coefficients besides the normal and tangential fracture compliances may be different from zero. In the following, we examine the dynamic behaviour and importance of these nonzero excess compliances for the TLM, prior to analysing their influence on the anisotropic seismic response of the fractured medium.

3 SENSITIVITY ANALYSIS

We consider a model that is composed of a water-saturated quartz sandstone with a set of regularly distributed vertical fractures of uniform aperture (Fig. 1). The physical properties of the solid grains, pore fluid, and fractures, as well as the aperture and separation of the fractures were chosen following the work of Rubino *et al.* (2015) and are listed in Table 1.

3.1 Analysis of the magnitude of the TLM excess compliances

3.1.1 Frequency dependence

To evaluate the expressions obtained for the elements of the TLM fracture excess compliance matrix $\delta \mathbf{S}(\omega)$, we first consider for the dry background rock a porosity $\phi_b = 0.15$ and a bulk modulus $K_b^{\text{dry}} = 17.2$ GPa, which are representative of a well consolidated quartz sandstone (Rubino *et al.* 2012). The background shear modulus μ_b is computed using the following empirical relation (Picket 1963)

$$\frac{\mu_b}{K_b^{\text{dry}}} = \frac{\mu_g}{K_g}, \tag{21}$$

that in this case yields a value of $\mu_b = 20.45$ GPa. The permeability of the background is calculated according to the Kozeny–Carman relation (Mavko *et al.* 2009)

$$\kappa_b = \frac{\beta d^2 \phi_b^3}{(1 - \phi_b)^2}, \tag{22}$$

Table 1. Solid grain, pore fluid and fracture properties used in the parametric analysis (Rubino *et al.* 2015).

Solid grain bulk modulus (quartz)	K_g	[GPa]	37
Solid grain shear modulus	μ_g	[GPa]	44
Solid grain density	ρ_g	[g cm^{-3}]	2.65
Water bulk modulus	K_f	[GPa]	2.25
Water viscosity	η	[cP]	1
Water density	ρ_f	[g cm^{-3}]	1.09
Fracture porosity	ϕ_c	[–]	0.9
Fracture dry bulk modulus	K_c^{dry}	[GPa]	0.024
Fracture shear modulus	μ_c	[GPa]	0.012
Fracture permeability	κ_c	[D]	100
Fracture aperture	L_c	[cm]	0.04
Fracture separation	L	[cm]	10
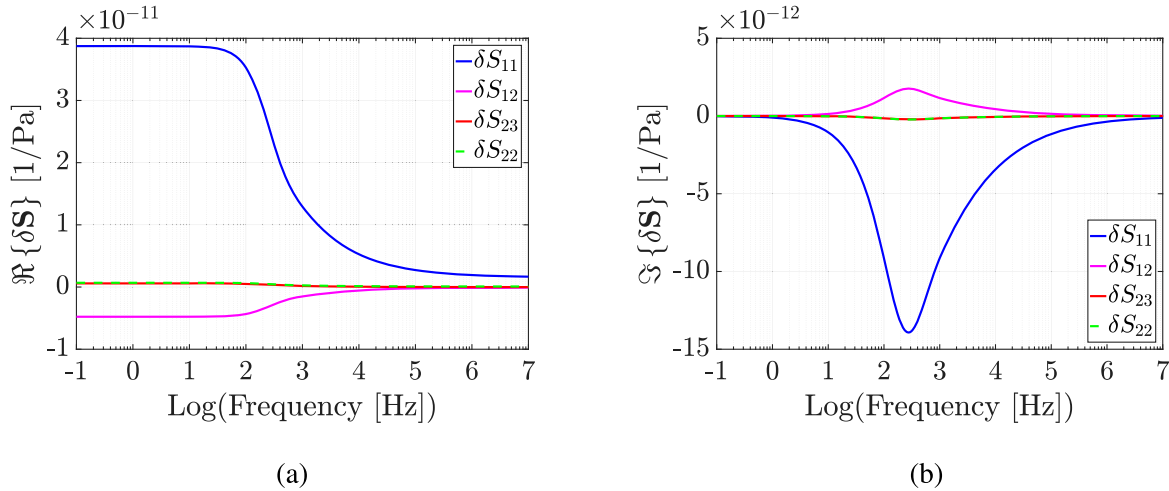
Figure 2. (a) Real and (b) imaginary parts of the dynamic elements of the TLM excess compliance matrix as functions of frequency.

where β is a geometric factor and d is the average grain diameter. Taking $\beta = 0.003$ and $d = 80\ \mu$m (Rubino & Holliger 2012), we have κ_b = 89.7 mD for the permeability of the background.

The excess compliances δS_{44} and δS_{55} are real-valued and frequency-independent, as we observe from eqs (17) and (18), combined with eqs (A7), (A8), (A20) and (A21), that they only depend on the shear modulus of both the background rock and the fractures, which are parameters that are not affected by FPD. The element δS_{55} is related to the tangential fracture compliance η_T of the classical LST, as can be seen by comparing eqs (2) and (10). This parameter represents the additional tangential compliance that the fractures add to the background when the rock is subjected to a pure shear stress on a plane parallel to the fractures. In this case, it takes the value $\delta S_{55}=3.33\times 10^{-10}$ Pa^{-1}, which is an order-of-magnitude greater than the corresponding element of the background rock compliance matrix $S_{55}^b=4.89\times 10^{-11}$ Pa^{-1}. Conversely, the excess compliance δS_{44}, which is not considered in the LST approach, takes a value of $\delta S_{44}=1.96\times 10^{-13}$ Pa^{-1}, which is several orders-of-magnitude smaller than $S_{44}^b=4.89\times 10^{-11}$ Pa^{-1}. This element can therefore be neglected and, hence, the lower right quarters of both the TLM and LST excess compliance matrices become equivalent.

The magnitude of both the real and imaginary parts of the excess compliance δS_{11} are significantly greater than those of the remaining excess compliances (Fig. 2). This feature is expected since δS_{11} is related to the fracture normal compliance η_N of the LST, as can be seen by comparing the structure of the excess compliance matrix $\delta \mathbf{S}$ of eq. (10) with that given in eq. (2). This parameter relates the discontinuity in the solid displacement between the boundaries of the fractures to the stresses across the fractures, both in the direction normal to the fracture plane (Schoenberg 1980). For a homogeneous fracture of finite thickness, this displacement discontinuity is associated to the fracture deformation in the fracture normal direction (Barbosa *et al.* 2017). Therefore, the excess compliance δS_{11} represents the mechanical compliance added by the fractures to the background in the direction perpendicular to the fractures when the rock is subjected to stress along this direction. As in the work of Rubino *et al.* (2015) for a frequency-dependent fracture normal compliance, we observe that the real part of δS_{11} in the high-frequency limit, referred to as δS_{11}^u, is at its minimum. As in this limiting case there is no fluid pressure exchange between fractures and their embedding background, the stiffening effect of the saturating fluid in the fractures is maximal. This effect makes the effective mechanical compliance of the saturated fractures to be minimal in the unrelaxed state. In the low-frequency limit, the situation is different since a large amount of fluid flows from the fractures into the background during the compressional cycle of a propagating wave in order to fully equilibrate the pore fluid pressure. Thus, the stiffening effect of the saturating fluid reduces to its minimum, which, in turn, results in a maximal deformation of the fractures and, hence, a substantial increase in the real part of the excess compliance δS_{11}, referred to as δS_{11}^r

(Fig. 2a). In both frequency limits the imaginary part of δS_{11} is negligible, which is expected since the TLM in both the relaxed and unrelaxed states behaves as an equivalent elastic solid. Nevertheless, for frequencies between these two limiting cases, energy dissipation due to FPD can take place, leading to seismic attenuation and velocity dispersion. In this frequency range the real part of the excess compliance δS_{11} exhibits a transition from its largest value δS_{11}^r to its lowest value δS_{11}^u (Fig. 2a). Moreover, the imaginary part of this element reaches its maximum at a certain characteristic frequency f_c within the transitional frequency range (Fig. 2b), which is where the dispersion of the real part is maximal (Fig. 2a).

In the high-frequency limit, the real part of the additional excess compliances are negligible within a long-wavelength approximation (Fig. 2a). Since both the fractures and the background can be locally modeled as elastic equivalent solids, the effective anisotropic response of the fractured medium is well represented by the classical elastic LST approach. This result is agreement with the work of Li *et al.* (2014) for a single elastic fracture of finite thickness. Although in the low-frequency limit the real parts of the additional excess compliances are at their maxima, only that of δS_{12} reaches a non-negligible value that may have an impact on the calculation of the anisotropic effective response of the fractured rock. Its value in this case is $\delta S_{12}^r = -4.78 \times 10^{-12}$ Pa^{-1}, which is larger in magnitude than that of the corresponding compliance of the background rock $S_{12}^b = -2.84 \times 10^{-12}$ Pa^{-1}. Finally, we observe that the imaginary parts of all the excess compliances become maximal at the characteristic frequency f_c (Fig. 2b), as expected since in our model all the elements are assumed to have the same fluid pressure relaxation behaviour (eq. 5). Once again, the parameter δS_{12} is the only additional excess compliance that has a maximum of its imaginary part that may be non-negligible.

3.1.2 Dependence on background physical properties

The frequency-dependent effective anisotropic response of fractured media is expected to depend on the characteristics of the background, where most of the energy dissipation due to FPD prevails (Rubino *et al.* 2014). Up to now, we have considered a particular fractured rock sample. Here, we evaluate the magnitude of the frequency-dependent elements of the TLM excess compliance matrix in the low-frequency limit and at the characteristic frequency of the FPD process f_c as functions of different background properties. We parametrize our sensitivity analysis as functions of porosity and dry bulk modulus of the background. For the porosity ϕ_b, we consider the range between 0, which approximates a massive quartzite, and 0.35, which is near the typical value of the critical, or maximum, porosity sandstones (Mavko *et al.* 2009). Then, the dry bulk modulus K_b^{dry} can be related to the porosity ϕ_b by means of a model proposed by Pride (2005)

$$K_b^{\text{dry}} = K_g \left(\frac{1-\phi_b}{1+c\phi_b} \right),$$ (23)

where c is the 'consolidation parameter', which characterizes the degree of cohesion between the solid grains of the porous rock. For consolidated sandstones, it is expected that this parameter ranges from $c = 2$ (extremely consolidated) to $c = 20$ (poorly consolidated) depending on certain properties of the microstructure (Pride 2005). Thus, we vary the consolidation parameter between these values and use eq. (23) to compute, for each value of the background porosity ϕ_b, the corresponding value of the dry bulk modulus K_b^{dry}. The associated shear modulus μ_b and permeability κ_b are computed for each pair (ϕ_b, K_b^{dry}) following the relations given in eqs (21) and (22), respectively. To illustrate how significant the value of the excess compliances can be, we normalize them with respect to their corresponding elements of the background compliance matrix. In all cases, the set of free parameters (ϕ_b, K_b^{dry}) are bounded by those of the model described by eq. (23) with the upper bounds corresponding to the very strongly consolidated case ($c = 2$) and the lower ones to the poorly consolidated case ($c = 20$). All the figures regarding the analysis of a certain variable as a function of these properties will be displayed between these curves.

In the relaxed case, δS_{11}^r increases with respect to S_{11}^b as the porosity and consolidation of the background rock increases (Fig. 3a). For very low porosities (less than 10 per cent), there is little exchange of fluid between these regions due to the limited pore space volume of background material involved, although the compressibility contrast between fractures and the embedding background is large due to the high bulk modulus of the latter. Consequently, the fracture exhibits relatively small additional deformation due to FPD, and the corresponding fracture compliance is relatively small. High background porosity, on the other hand, favors the pore fluid exchange and, hence, the additional fracture deformation due to this process increases. In this case, the fracture is therefore more compliant. This effect is enhanced by the increase in consolidation of the background material as it implies an increase in its bulk modulus, and thus, a larger compressibility contrast between fractures and background. Concerning the additional excess compliances of the TLM, while δS_{22}^r and δS_{23}^r do not exceed 15 per cent of their corresponding background compliances in most cases, δS_{12}^r can take significant values of up to 1.6 times the background compliance S_{12}^b (Figs 3b–d).

At the FPD characteristic frequency f_c, the magnitude of the imaginary part of δS_{11} increases with increasing porosity and consolidation of the background rock (Fig. 4a). Within the framework of the LST, this parameter encodes energy dissipation and the consequent seismic attenuation due to FPD for a propagation direction perpendicular to the fractures (Rubino *et al.* 2015). Therefore, it is expected to be larger in magnitude than those of the remaining elements of the TLM excess compliance matrix as we observe in Fig. 2b. For this reason, we compare the magnitudes of the imaginary parts of δS_{12}, δS_{22} and δS_{23} with that of δS_{11}. While the excess compliance δS_{12} takes values of up to 30 per cent of δS_{11} for its imaginary part (Fig. 4b), those of the excess compliances δS_{22} and δS_{23} do not exceed 7 per cent of that of δS_{11} (Figs 4c and d, respectively).
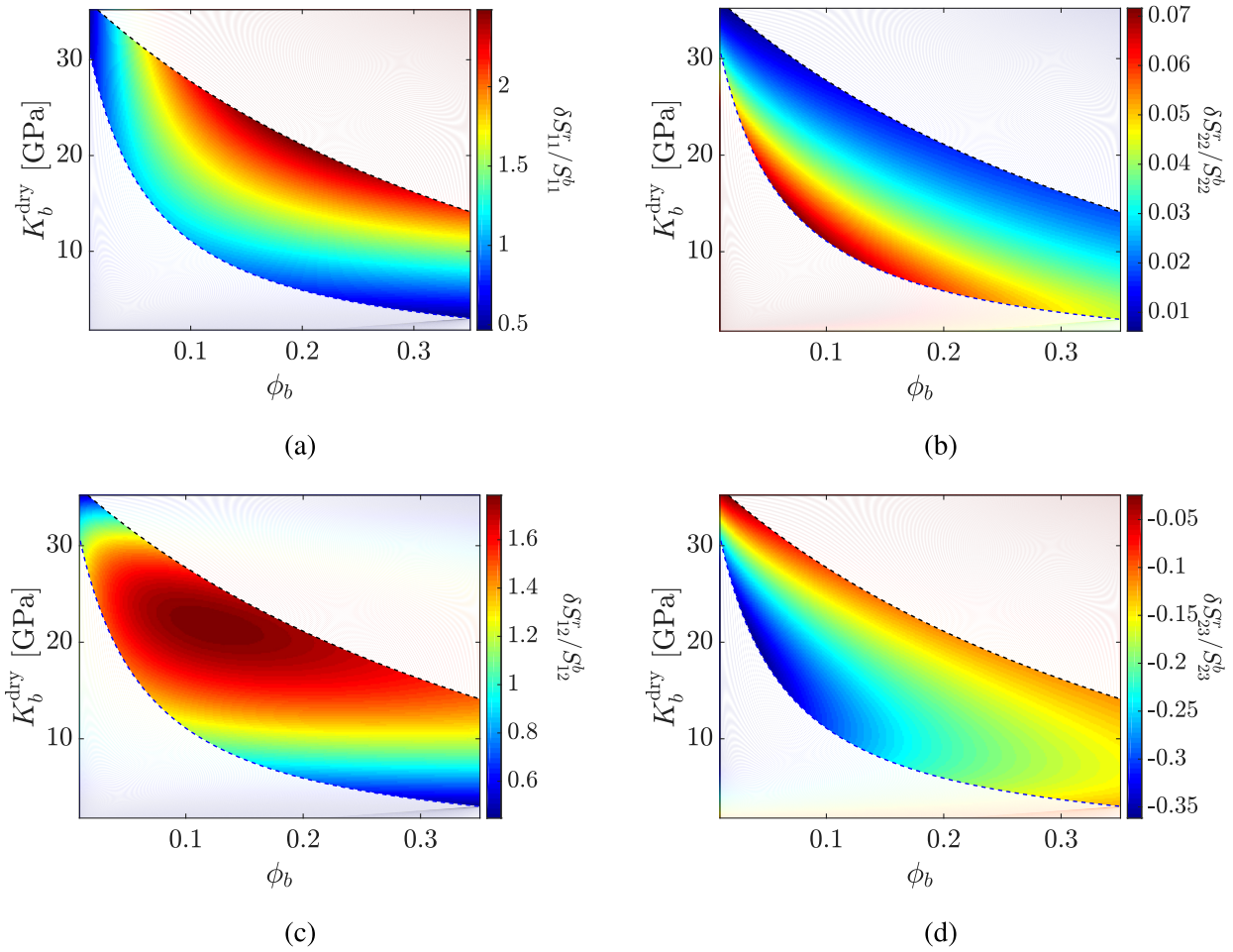
(a)

(b)

(c)

(d)

Figure 3. Ratio between the excess compliances of the TLM and their corresponding background compliances for the relaxed case: (a) $\delta S_{11}^r/S_{11}^b$, (b) $\delta S_{22}^r/S_{22}^b$, (c) $\delta S_{12}^r/S_{12}^b$ and (d) $\delta S_{23}^r/S_{23}^b$ as functions of the porosity and dry bulk modulus of the background. The upper and lower dashed lines are computed from eq. (23) for strongly and weakly consolidated sandstones, respectively.

3.2 Physical meaning of the excess compliance δS_{12}

The above analysis suggest that, in the presence of FPD effects, the anisotropic seismic attenuation behaviour of the fractured rock mass can be affected by the typically neglected frequency-dependent excess compliance δS_{12}. In the following, we explore the significance of δS_{12} considering again the particular rock sample of Section 3.1.1.

3.2.1 Anisotropic Poisson coefficient v_{12}

Considering an uniaxial stress applied along the x_2-axis (parallel to the fractures), we can define an anisotropic Poisson ratio that compares the resultant deformation in the x_1-direction (perpendicular to the fractures) with that in the x_2-direction (Mavko *et al.* 2009)

$$v_{12} = -\frac{\text{deformation along the } x_1 \text{ axis}}{\text{deformation along the } x_2 \text{ axis}}. \tag{24}$$

We compute this parameter in terms of the effective compliances, for the TLM, as

$$v_{12}^{\text{TLM}}(\omega) = -\Re\left\{\frac{S_{12}(\omega)}{S_{22}(\omega)}\right\} = -\Re\left\{\frac{S_{12}^b + \delta S_{12}(\omega)}{S_{22}^b + \delta S_{22}(\omega)}\right\}, \tag{25}$$

and for the LST approach as

$$v_{12}^{\text{LST}}(\omega) \equiv -\frac{S_{12}^b}{S_{22}^b}, \tag{26}$$

which does not vary with the frequency and is equal to the isotropic Poisson ratio of the background. In the high-frequency limit, the excess compliance δS_{12} takes the value $\delta S_{12}^u = -7.47 \times 10^{-14}$ Pa^{-1}, which is negligible with respect to its corresponding background compliance S_{12}^b. A similar result is obtained for the excess compliance δS_{22}, as it takes the high-frequency value $\delta S_{22}^u = 8.67 \times 10^{-13}$ Pa^{-1} and its
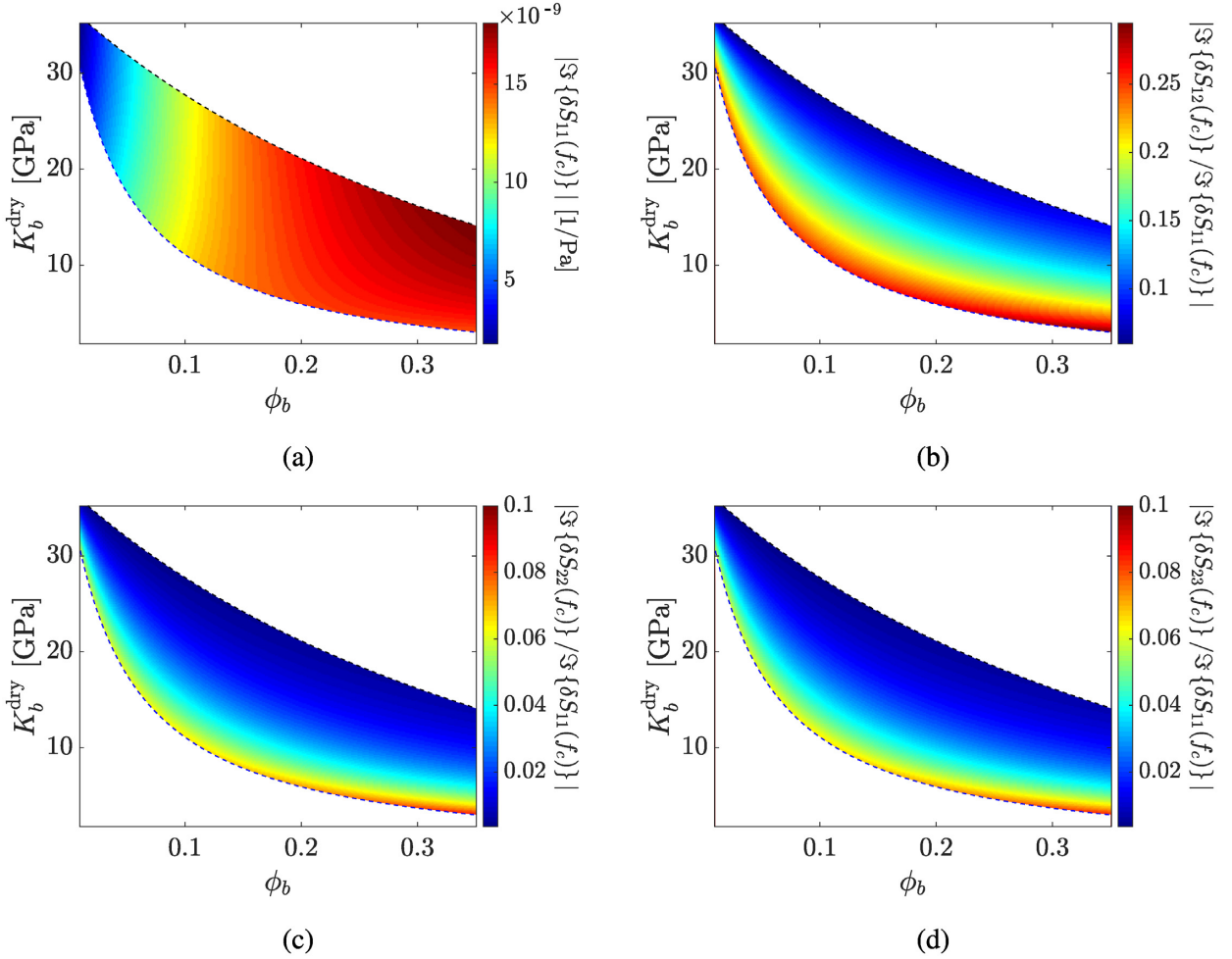
Figure 4. (a) Absolute value of the imaginary part, at the FPD characteristic frequency f_c, of the excess compliance δS_{11} and the corresponding imaginary parts of (b) δS_{12}, (c) δS_{22} and (d) δS_{23} normalized with respect to that of δS_{11} as functions of background porosity and dry bulk modulus. The upper and lower dashed lines are computed from eq. (23) for strongly and weakly consolidated sandstones, respectively.

corresponding background compliance is $S_{22}^b = 2.16 \times 10^{-11}$ Pa^{-1}. Therefore, the anisotropic Poisson ratio for the TLM in this limit $\left(\nu_{12}^{\text{TLM}}\right)^u$ also approximates the value of the isotropic Poisson ratio of the background

$$\left(\nu_{12}^{\text{TLM}}\right)^u \simeq -\frac{S_{12}^b}{S_{22}^b}. \tag{27}$$

However, the real part of the excess compliance δS_{12} assumes a non-negligible value δS_{12}^r in the low-frequency limit that is greater than the corresponding element of the compliance matrix of the background S_{12}^b. Since the excess compliance δS_{22} in this limit is $\delta S_{22}^r = 6.82 \times 10^{-13}$ Pa^{-1}, which is much smaller than the corresponding element of the background compliance matrix, the Poisson ratio for the TLM in the relaxed state $\left(\nu_{12}^{\text{TLM}}\right)^r$ can thus be approximated by

$$\left(\nu_{12}^{\text{TLM}}\right)^r \simeq -\frac{S_{12}^b + \delta S_{12}^r}{S_{22}^b} = \left(\nu_{12}^{\text{TLM}}\right)^u - \frac{\delta S_{12}^r}{S_{22}^b}. \tag{28}$$

The values that ν_{12}^{TLM} takes in the relaxed and unrelaxed regimes differ significantly (Fig. 5a). The increase in the anisotropic Poisson ratio for the TLM as we move towards lower frequencies is due to FPD and can be directly associated with the excess compliance δS_{12} (eq. 28). In the unrelaxed state there is no fluid pressure communication between the fractures and the background rock, and thus, when the fractured rock is subjected to uniaxial stress in the x_2-direction, the deformation of the fractures is negligible in the x_1-direction. For this reason, the fractured rock has no additional deformation due to the presence of the fractures in this direction and the anisotropic Poisson ratio for both models is equal to the isotropic one of the background rock. However, in the relaxed state, the hydraulic coupling between the fractures and the background allows the fractures to open, that is, to increase their aperture due to FPD, when the rock mass is subjected to uniaxial compression in a direction parallel to the plane of the fractures. Such fracture behaviour induces an additional deformation in the direction normal to the fractures and, consequently, an increase in the anisotropic Poisson ratio ν_{12}. The described coupling between orthogonal deformations due to FPD cannot be modeled with the LST approach. This effect prevails when a seismic wave propagates obliquely to the fractures and
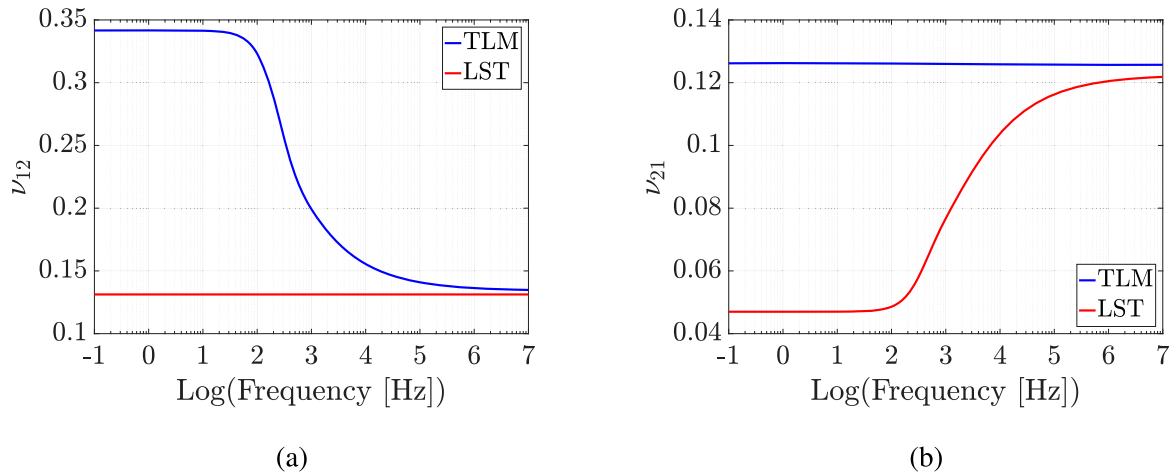
Figure 5. Anisotropic Poisson ratios (a) ν_{12} and (b) ν_{21} as functions of frequency for a rock sample with $\phi_b = 0.15$ and $K_b^{dry} = 17.2$ GPa.

the induced stress field has a component parallel to the fractures. Due to the symmetry of the model geometry, a similar analysis could be performed for a compression applied in the x_3-direction, leading to the same results.

3.2.2 Anisotropic Poisson coefficient ν_{21}

We now consider the case of uniaxial stress applied along the symmetry axis x_1 (perpendicular to the fractures). In this case, we can specify an anisotropic Poisson ratio ν_{21} that relates the deformation in the x_2-direction with the deformation in the direction of the applied stress (Mavko *et al.* 2009)

$$\nu_{21} = -\frac{\text{deformation along the } x_2 \text{ axis}}{\text{deformation along the } x_1 \text{ axis}}. \tag{29}$$

For the TLM we compute this parameter as

$$\nu_{21}^{\text{TLM}}(\omega) = -\Re\left\{\frac{S_{12}(\omega)}{S_{11}(\omega)}\right\} = -\Re\left\{\frac{S_{12}^b + \delta S_{12}(\omega)}{S_{11}^b + \delta S_{11}(\omega)}\right\}, \tag{30}$$

and for the LST as

$$\nu_{21}^{\text{LST}}(\omega) = -\Re\left\{\frac{S_{12}^b}{S_{11}^b + \delta S_{11}(\omega)}\right\}. \tag{31}$$

In the high-frequency limit, the difference observed between the two models (Fig. 5b) is only due to the presence of the excess compliance δS_{12} as can be seen by comparing the following limiting values

$$\left(\nu_{21}^{\text{TLM}}\right)^u = -\frac{S_{12}^b + \delta S_{12}^u}{S_{11}^b + \delta S_{11}^u}, \tag{32}$$

and

$$\left(\nu_{21}^{\text{LST}}\right)^u = -\frac{S_{12}^b}{S_{11}^b + \delta S_{11}^u}. \tag{33}$$

Since δS_{12}^u is negligible with respect to S_{12}^b, the difference between these two anisotropic Poisson ratios is very small. Moreover, as in this case $\delta S_{11}^u = 1.55 \times 10^{-12}$ Pa^{-1} is much smaller than its corresponding background compliance S_{11}^b, both Poisson ratios approach the isotropic value of the background. However, in the low-frequency limit, the difference between these parameters is significant (Fig. 5b). Although the limiting expressions

$$\left(\nu_{21}^{\text{TLM}}\right)^r = -\frac{S_{12}^b + \delta S_{12}^r}{S_{11}^b + \delta S_{11}^r}, \tag{34}$$

and

$$\left(\nu_{21}^{\text{LST}}\right)^r = -\frac{S_{12}^b}{S_{11}^b + \delta S_{11}^r}, \tag{35}$$

are similar to eqs (32) and (33), as δS_{12}^r is larger than its corresponding background compliance S_{12}^b, the anisotropic Poisson ratio for the TLM is greater than that for the LST approach. When the fractured rock is compressed in a direction perpendicular to the plane of the fractures, the fractures tend to close. Since in the relaxed state this aperture decrease is maximal due to FPD, the elongation of the fractures

in a perpendicular direction is significant. Therefore, the deformations of the fractured rock perpendicular and parallel to the plane of the fractures are expected to be coupled. This coupling between orthogonal deformations is not accounted for by the LST as we observe that the anisotropic Poisson ratio obtained with this model is very small, implying that the deformation parallel to the fractures is almost negligible. The difference between the high- and low-frequency values of ν_{21}^{LST} is only related to the variation of the normal excess compliance δS_{11} with frequency (Fig. 2a). However, the TLM captures the FPD coupling effect, as the frequency-dependent behaviour of δS_{11} is compensated by the excess compliance δS_{12}. This compensation implies that $\left(\nu_{21}^{\mathrm{TLM}}\right)^r \simeq \left(\nu_{21}^{\mathrm{TLM}}\right)^u$. Due to the symmetry of the model geometry, a similar analysis could be performed for the deformation parallel to the fractures in the x_3-direction, leading to the same results.

3.3 Impact of the TLM excess compliances on seismic signatures

The results presented so far have been focused on the magnitudes of the excess compliances of the TLM. Although these results allow us to analyse how the FPD process affects the excess compliances that are not accounted for in the classical LST approach, the impact of these parameters on the anisotropic seismic response of fractured rocks remains to be clarified. In this section, we study this influence by considering two different stiffness matrices to model the effective response of a porous rock with vertical parallel fractures: one corresponding to the TLM, $\mathbf{C}(\omega)$, and the other, $\tilde{\mathbf{C}}(\omega)$, based on a LST approach. The first one, given in eq. (5), has all the fracture excess compliances included. The second one is obtained by inverting the effective compliance matrix $\tilde{\mathbf{S}}(\omega)$, which is given by

$$\tilde{\mathbf{C}}(\omega) = \left[\tilde{\mathbf{S}}(\omega)\right]^{-1} = \left[\mathbf{S}^b + \delta\tilde{\mathbf{S}}(\omega)\right]^{-1}, \tag{36}$$

where the excess compliance matrix $\delta\tilde{\mathbf{S}}(\omega)$ has the same structure as that in eq. (2), with the fracture normal compliance η_N given by $\delta S_{11}(\omega)$ (eq. 11) and the fracture tangential compliance η_T equal to the coefficient δS_{55} (eq. 18).

3.3.1 P- and SV-wave phase velocities

We first analyse the phase velocity of the fundamental propagation modes in TI media, that is, quasi-longitudinal (P), quasi-shear (SV) and pure shear (SH), as functions of the angular frequency ω and the angle of incidence θ. The latter is the angle between the direction of wave propagation and the x_1-axis of symmetry (Fig. 1). The phase velocities corresponding to the TLM can be obtained from the components of the complex-valued and frequency-dependent effective stiffness matrix $\mathbf{C}(\omega)$. Since our aim is to study FPD effects and SH waves are not affected by this process (Barbosa *et al.* 2017), we restrict our analysis to quasi-*P* and quasi-SV wave propagation in the x_1-x_3 plane. Therefore, we first compute their corresponding complex velocities as follows (Mavko *et al.* 2009)

$$v_{\mathrm{P}}^2(\omega, \theta) = \frac{C_{22}(\omega)\sin^2\theta + C_{11}(\omega)\cos^2\theta + C_{55} + \sqrt{C^*(\omega, \theta)}}{2\langle\rho\rangle}, \tag{37}$$

$$v_{\mathrm{SV}}^2(\omega, \theta) = \frac{C_{22}(\omega)\sin^2\theta + C_{11}(\omega)\cos^2\theta + C_{55} - \sqrt{C^*(\omega, \theta)}}{2\langle\rho\rangle}, \tag{38}$$

where $\langle\rho\rangle = h_b\rho_b + h_c\rho_c$ is the average bulk density, in which $\rho_b = \phi_b\rho_{fb} + (1 - \phi_b)\rho_g$ and $\rho_c = \phi_c\rho_{fc} + (1 - \phi_c)\rho_g$ are the bulk densities of the background rock and the fractures, respectively. The quantity C^* is given by

$$C^*(\omega, \theta) = \left\{[C_{22}(\omega) - C_{55}]\sin^2\theta - [C_{11}(\omega) - C_{55}]\cos^2\theta\right\}^2 + [C_{12}(\omega) + C_{55}]^2\sin^2 2\theta. \tag{39}$$

Subsequently, we compute the phase velocity of each mode in terms of its corresponding complex-valued velocities

$$\frac{1}{V_m(\omega, \theta)} = \Re\left\{\frac{1}{v_m(\omega, \theta)}\right\}, \tag{40}$$

where the subscript m refers to either P or SV waves. The corresponding phase velocities $\tilde{V}_{\mathrm{P}}(\omega, \theta)$ and $\tilde{V}_{\mathrm{SV}}(\omega, \theta)$ for the LST approach are computed following eqs (37)–(40) using the stiffness coefficients of the frequency-dependent stiffness matrix $\tilde{\mathbf{C}}(\omega)$. To quantify the discrepancies between these two models, we compute for both P and SV waves the quantity

$$\Delta V_m(\omega, \theta) = \frac{\left|V_m(\omega, \theta) - \tilde{V}_m(\omega, \theta)\right|}{V_m(\omega, \theta)} \times 100 \, \mathrm{per\,cent}, \tag{41}$$

for different combinations of the background properties ϕ_b and K_b^{dry} and then determine its maximum for a given frequency ω and a variable incidence angle

$$\Delta V_m^{\max}(\omega) = \max_{0 \leq \theta \leq \pi/2} \Delta V_m(\omega, \theta). \tag{42}$$

The maximum relative difference in P-wave velocity between the TLM and the LST in the low-frequency limit can be significant, reaching values of up to 12 per cent for relatively poorly consolidated materials (Fig. 6a). In addition, these discrepancies prevail for angles of incidence ranging mainly from 25° to 35° (Fig. 6b). When a compressional seismic wave propagates obliquely to the plane of the fractures, its associated stress field has components both normal and parallel to this plane. If the additional excess compliances are taken into account, the parallel components of the stress will induce deformation of the fractures due to FPD in a direction perpendicular to the fracture plane. This
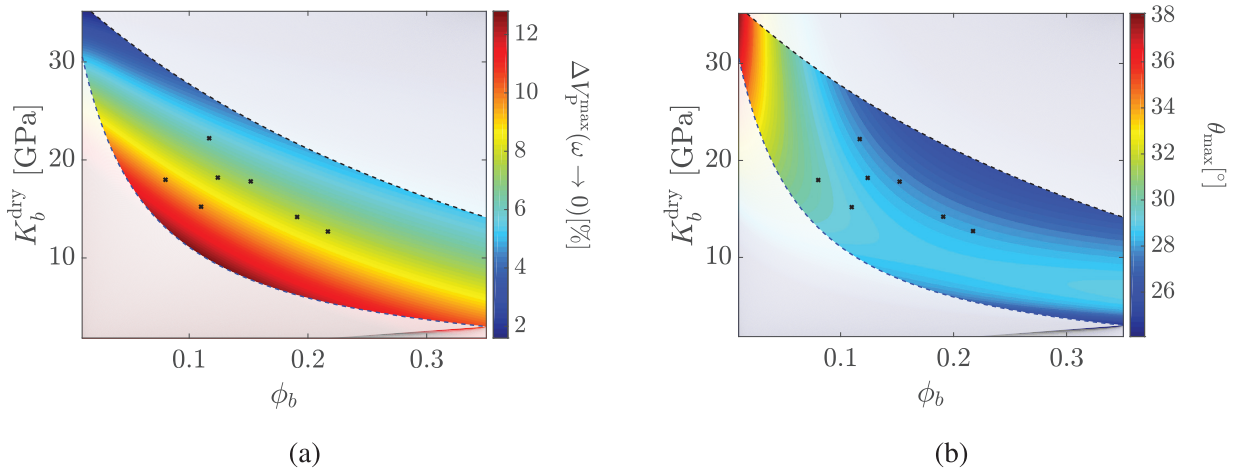
Figure 6. (a) Maximum value of ΔV_P (θ) for the low-frequency limit. (b) Angle of incidence θ_{max} where ΔV_P reaches its maximum. The upper and lower dashed lines are computed from eq. (23) for strongly and weakly consolidated sandstones, respectively. The black dots correspond to porosities and bulk moduli of various dry sandstones listed in Table 2.

Table 2. Porosities and bulk moduli of dry sandstones documented in the literature (Gibiansky & Torquato 1998).

	ϕ_b	K_b^{dry} [GPa]
Sandstone 1 (Travis Peak)	0.08	18
Sandstone 2 (Chugwater)	0.11	15.2
Sandstone 3 (Green River)	0.117	22.2
Sandstone 4 (Cabinda)	0.124	18.2
Sandstone 5 (Tensleep)	0.152	17.8
Sandstone 6 (Berea)	0.191	14.2
Sandstone 7 (Gulf Coast)	0.217	12.7
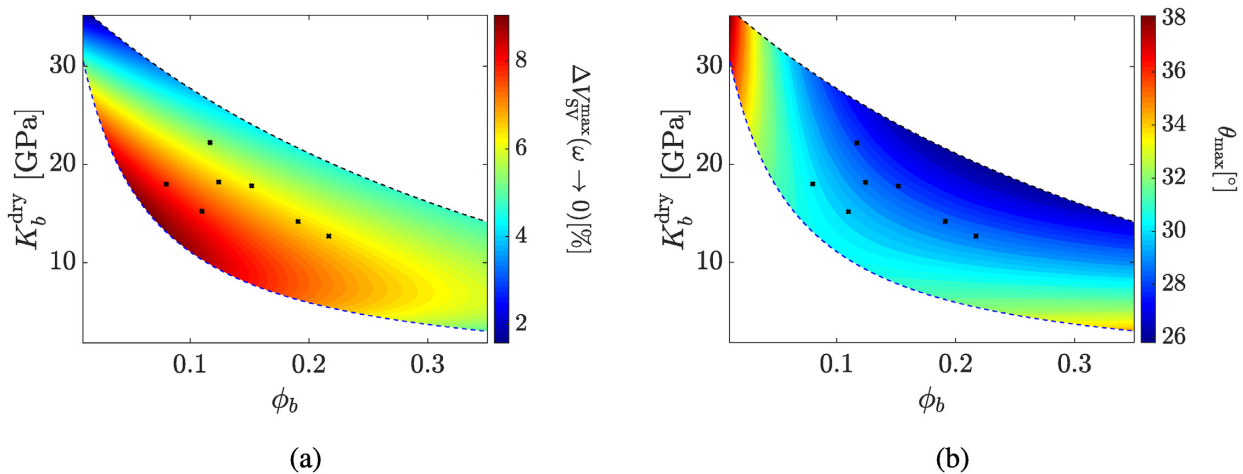
Figure 7. (a) Maximum value of ΔV_{SV} (θ) for the relaxed case. (b) Angle of incidence θ_{max} where ΔV_{SV} reaches its maximum. The upper and lower dashed lines are computed from eq. (23) for strongly and weakly consolidated sandstones, respectively. The black dots correspond to porosities and bulk moduli of various dry sandstones listed in Table 2.

physical process gets particularly important for relatively poor consolidated rocks since the additional excess compliances become significant for this type of background material (Fig. 3). The result is that the phase velocities estimated with the TLM are different from those computed with the LST approach. For example, for a background composed of a typical Berea sandstone ($\phi_b = 0.191$, $K_b^{dry} = 14.2$ GPa), the maximum relative difference between the considered models is $\simeq 8$ per cent. This result indicates that the presence of the additional excess compliances has a non-negligible impact on the estimation of phase velocities for oblique incidence of compressional waves in the low-frequency limit. A similar result is obtained for the propagation of shear waves (Fig. 7). While the magnitude of the maximum relative difference is lower than that of the *P*-wave case, the maxima occur at slightly larger angles of incidence.
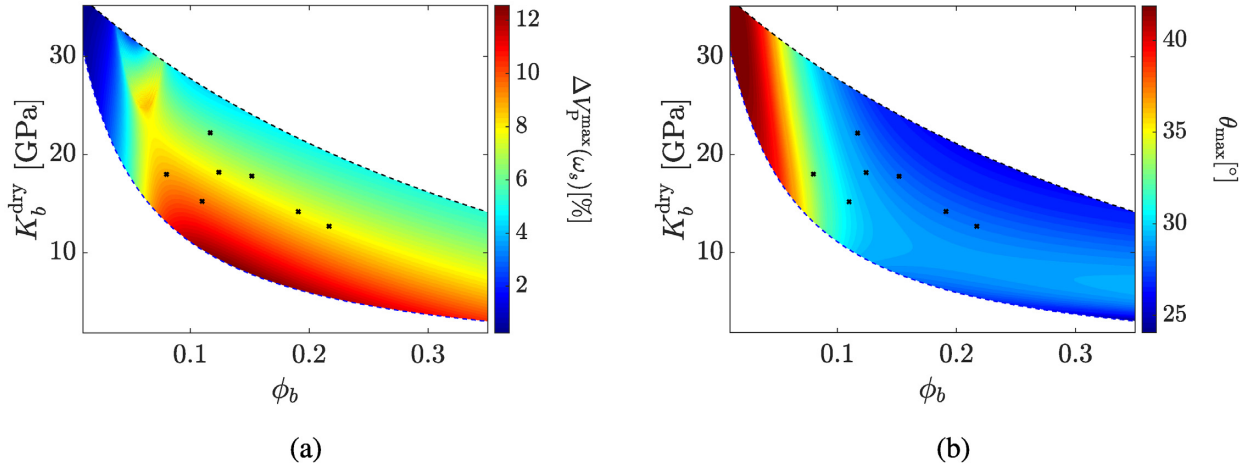
Figure 8. (a) Maximum value of $\Delta V_P(\theta)$ for a frequency $f_s = 30$ Hz ($\omega_s = 2\pi f_s$). (b) Angle of incidence $\theta_{\max}$ where ΔV_P reaches its maximum. The upper and lower dashed lines are computed from eq. (23) for strongly and weakly consolidated sandstones, respectively. The black dots correspond to porosities and bulk moduli of various dry sandstones listed in Table 2.

For a typical seismic frequency $f_s = 30$ Hz, the discrepancies in the *P*-wave velocity between the two models are smaller than those in the low-frequency limit, although they present a similar behaviour with respect to the porosity and bulk modulus of the dry background rock (Fig. 8). This result is expected since the additional excess compliances reach their maximum values in the relaxed state. The discrepancies between the TLM and the LST approach in the computation of longitudinal phase velocities decrease as frequency increases. However, we observe that for seismic frequencies these differences are still appreciable and the additional excess compliances are needed to fully describe the effective anisotropic response of the probed fractured rock mass.

3.3.2 Seismic attenuation due to wave-induced FPD

Proceeding in a similar fashion as for the analysis of phase velocities, we study the impact of the excess compliances on the *P*- and SV-wave attenuation due to FPD between fractures and background. With this goal in mind, we compute the inverse quality factors Q_m^{-1} and $\tilde{Q}_m^{-1}$, $m = P$, SV, for the TLM and the LST approach, respectively, as functions of the angular frequency ω and the angle of incidence θ (Krzikalla & Müller 2011)

$$Q_m^{-1}(\omega, \theta) = \frac{\Im\left\{v_m^2(\omega, \theta)\right\}}{\Re\left\{v_m^2(\omega, \theta)\right\}}, \tag{43}$$

$$\tilde{Q}_m^{-1}(\omega, \theta) = \frac{\Im\left\{\tilde{v}_m^2(\omega, \theta)\right\}}{\Re\left\{\tilde{v}_m^2(\omega, \theta)\right\}}. \tag{44}$$

To quantify the discrepancies between the inverse of the quality factors obtained with each model, we compute the relative difference ΔQ_m^{-1}

$$\Delta Q_m^{-1}(\theta) = \frac{\max_\omega\left\{\tilde{Q}_m^{-1}(\omega, \theta)\right\} - \max_\omega\left\{Q_m^{-1}(\omega, \theta)\right\}}{\max_\omega\left\{Q_m^{-1}(\omega, \theta)\right\}}. \tag{45}$$

Please note that, in the calculation of eq. (45), the inverse of the quality factors Q_P^{-1} and $\tilde{Q}_P^{-1}$ are computed at the frequencies of their corresponding maxima ω_c and $\tilde{\omega}_c$, respectively, as we have verified that the difference between these frequencies is relatively small.

For normal incidence ($\theta = 0°$), in both the TLM and the LST approaches the amplitude of the *P*-wave attenuation peak decreases as the consolidation of the background rock decreases (compare Figs 9a and b). This decrease is due to the fact that a well consolidated porous rock with fractures exhibits a larger compressibility contrast between the fractures and their embedding background than a poorly consolidated one. Therefore, the induced fluid pressure gradients and the associated seismic attenuation due to FPD are stronger for well consolidated background rocks. If we now compare the results obtained for each model, we observe that the attenuation levels for the TLM are significantly smaller than those for the LST approach. This difference increases as the consolidation of the background decreases, reaching values of up to 80 per cent for the limiting case of poorly consolidated and high-porosity sandstones (Fig. 9c). In most cases though, it reaches values of up to 40 per cent, which is still of importance. These discrepancies are explained by the presence of the additional excess compliances in the TLM. For lower degrees of consolidation, the additional excess compliances attain their maximum values whereas the influence of the normal compliance is less significant (Fig. 4). When these excess compliances are not taken into account, the additional deformation normal to the fracture set due to the presence of the fractures increases, thus increasing the amplitude of the attenuation peak for the fractured rock. It is interesting to note that these additional compliances also influence the effective seismic response of the fractured medium even for a normally incident *P* wave. This can be explained by considering the analysis of the anisotropic Poisson ratio ν_{21} in Section 3.2.2. Therein,
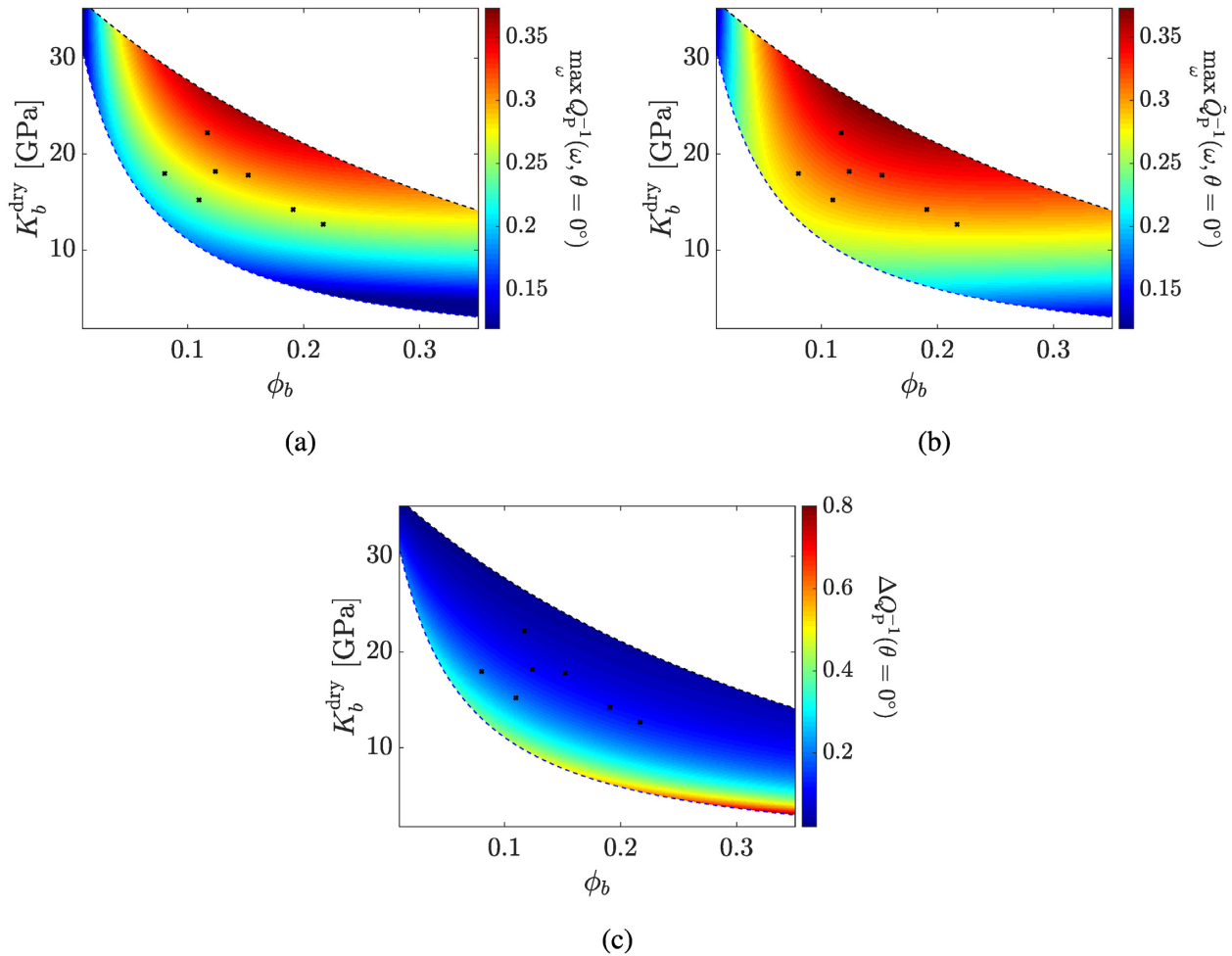
Figure 9. Maximum of the inverse *P*-wave quality factors (a) Q_P^{-1} and (b) $\tilde{Q}_P^{-1}$ for a *P*-wave propagating normally to the fractures ($\theta = 0°$) for the TLM and the LST, respectively. (c) Relative difference between these two models. The upper and lower dashed lines are computed from eq. (23) for strongly and weakly consolidated sandstones, respectively. The black dots correspond to porosities and bulk moduli of various dry sandstones listed in Table 2.

we show that the additional excess compliances account for the FPD effect on the coupling between deformations normal and parallel to the fractures when the fractured rock is subjected to stress only normal to the fracture planes.

For an oblique incidence ($\theta = 25°$), the amplitude of the *P*-wave attenuation peak for both the TLM and the LST approaches exhibit a similar behaviour as in the normal incidence case, although their magnitudes are smaller (Fig. 10). This decrease in amplitude prevails because maximum FPD occurs when the component of the induced stress field normal to the fractures attains its maximum, which occurs at normal incidence. However, the discrepancies between both models are larger for oblique incidence (Figs 9c and 10c). The relative differences reach values of up to 50 per cent in most cases, although they can be as large as 90 per cent for the limiting case of poorly consolidated and high-porosity sandstones. As opposed to the normal incidence case, the stress field induced by a *P*-wave propagating obliquely to the fractures has components in a direction parallel to the plane of the fractures. In this scenario, since the LST is not able to model the coupling due to FPD between orthogonal deformations of the fractured rock, the deformation normal to the fractures, and thus the pore fluid pressure gradients and the energy loss, are overestimated with this approach.

Finally, as expected for a relatively low incidence angle ($\theta = 25°$), the maximum attenuation corresponding to the propagation of a shear wave for both the TLM and the LST approaches is significantly lower than that of a compressional wave (Fig. 11). Although the relative differences between the two models still reach values of up to 90 per cent for low-porosity and relatively poorly consolidated sandstones, as opposed to the *P*-wave attenuation case, the LST exhibits a lower maximum attenuation than the TLM (Fig. 11c). This behaviour can be explained as follows. For an oblique incidence, the stress field induced by an SV wave has a component parallel to the fractures directed oppositely to that of a *P* wave. Therefore, the resultant deformations perpendicular and parallel to the fractures in the SV wave case have opposite sign, while in the *P*-wave case have the same sign. Since the LST is not able to model the coupling due to FPD between orthogonal deformations of the fractured rock, the deformation in the direction perpendicular to the fractures, and thus the pore fluid pressure gradients and the energy loss, are underestimated with this approach.
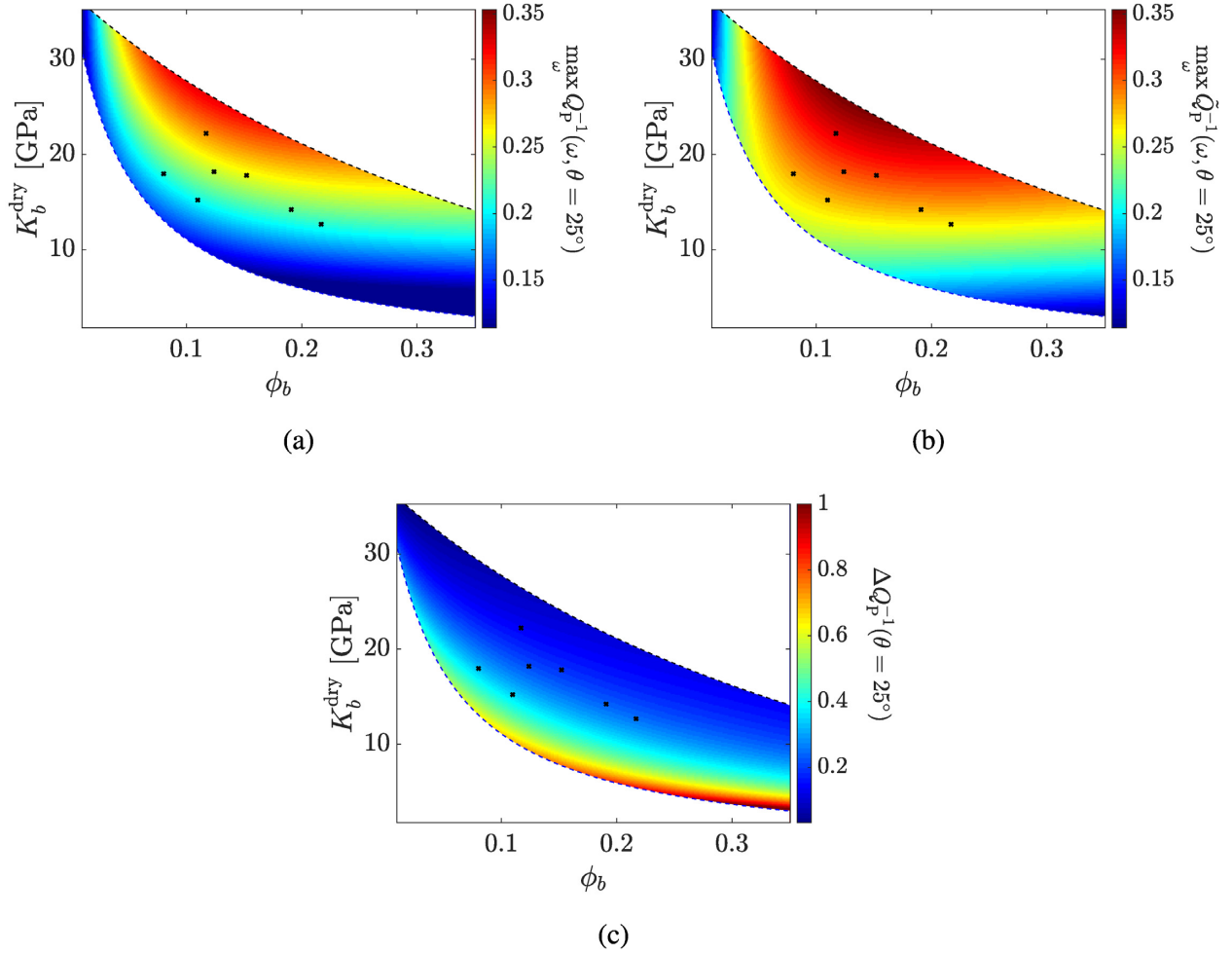
Figure 10. Maximum of the inverse *P*-wave quality factors (a) Q_P^{-1} and (b) $\tilde{Q}_P^{-1}$ for a *P*-wave propagating at an angle of incidence $\theta = 25°$ for both the TLM and the LST, respectively. (c) Relative difference between these two models. The upper and lower dashed lines are computed from eq. (23) for strongly and weakly consolidated sandstones, respectively. The black dots correspond to porosities and bulk moduli of various dry sandstones listed in Table 2.

4 DISCUSSION AND CONCLUSIONS

We modeled a fluid-saturated porous rock with aligned planar fractures of finite thickness as a sequence of very thin, highly porous and highly compliant poroelastic layers representing the fractures, alternating with relatively thick, much stiffer and less porous layers representing the background. The associated fracture excess compliance matrix for this TLM approach has additional elements to those present in the classical LST approximation and, due to FPD between fractures and their embedding background, they can be of significant importance. We explored the impact that these additional excess compliances have on the effective anisotropic response of the fractured medium for different combinations of dry background rock properties and analysed the observed behaviour.

The reason for only considering variations of the background rock properties is that, the way they were selected, they cover a wide range of fracture weaknesses, a parameter that provides information on the relative difference in stiffness between fractures and background, and thus, on the overall fractured rock characteristics. Besides, the physical and geometrical properties of the model were chosen so that the LST approach remains valid , that is, the thickness fraction h_c is of the order of 10^{-3} and the moduli K_c^{dry} and μ_c satisfy $K_c^{\mathrm{dry}}/K_g = O(h_c)$ and $\mu_c/K_g = O(h_c)$ (Brajanovski *et al.* 2005). The presented analytical derivation also allows to study the impact of varying fracture properties and type of fluid infill. Moreover, as the TLM is based on poroelastic Backus averaging, we can consider a pore fluid for the fractures different from that of the background rock. In the case that we increase the thickness fraction of the fractures or reduce the elastic moduli of their solid frame, so that the fractures become more compliant, the FPD effects as well as the relative differences in the anisotropic response between the TLM and the LST approach will increase. We would get the opposite result if we adjust the aforementioned parameters in a way that renders the fractures stiffer. Concerning the properties of the pore fluid, Kong *et al.* (2017) showed that, when the fractures are saturated with a very compressible fluid, such as gas, and the background rock is fully saturated with water, seismic attenuation may also be important. Although the analytical derivation presented in our work could be used to study the discrepancies between the TLM and LST approaches in such context, the corresponding analysis is beyond the scope of this paper and will be the subject of future work.
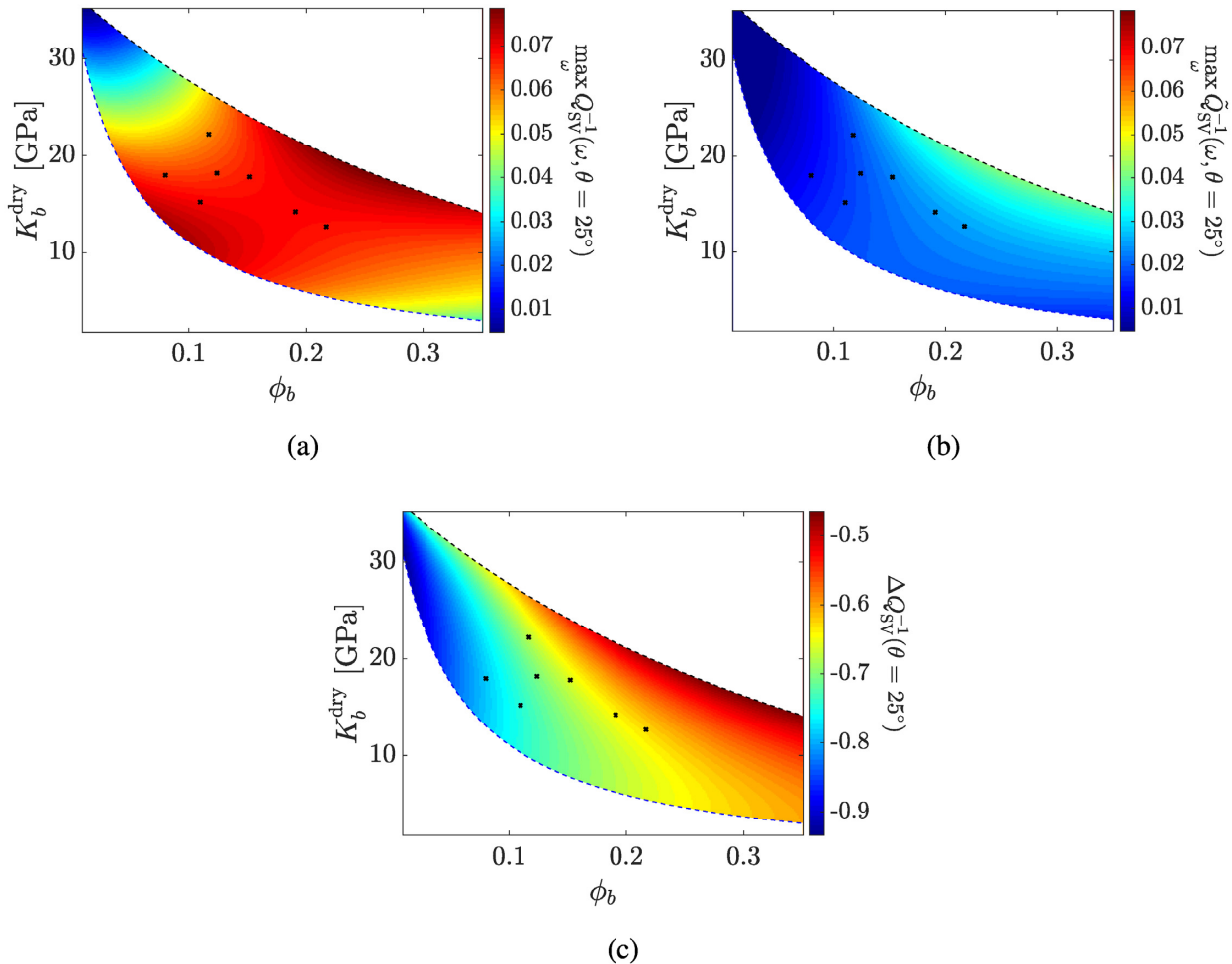
Figure 11. Maximum of the inverse SV-wave quality factors (a) Q_{SV}^{-1} and (b) $\tilde{Q}_{SV}^{-1}$ for an SV-wave propagating at an angle of incidence $\theta = 25°$ for both the TLM and the LST, respectively. (c) Relative difference between these two models. The upper and lower dashed lines are computed from eq. (23) for strongly and weakly consolidated sandstones, respectively. The black dots correspond to porosities and bulk moduli of various dry sandstones listed in Table 2.

Even though we presented the anisotropic seismic response through the analysis of phase velocities and attenuation, we examined other useful anisotropy indicators, such as the Thomsen parameters ϵ and δ (Thomsen 1986). We found, for both parameters in the low-frequency limit, that the relative differences between the TLM and LST approaches can reach values of up to 50 per cent, which indicates that the additional excess compliances could play an important role for the quantification of the overall anisotropy of fractured rocks. However, these results are not shown for the sake of brevity as, in the context of this work, they do not provide a further understanding on how FPD affects the accuracy of the LST approach.

The results shown in this work may have important practical implications. Several recent studies have attempted to characterize sets of vertically aligned fractures through measurements of both velocity and attenuation anisotropy obtained from surface seismic data (Verdon *et al.* 2009; Vizuett & Davis 2017; Chen & Innanen 2018). In these studies, the effective anisotropic response of the fractured reservoir is based on a LST approach and, to account for FPD effects, the real-valued fracture compliances of the classical LST are replaced with complex-valued and frequency-dependent ones (Bakulin *et al.* 2000; Chichinina *et al.* 2006; Guo *et al.* 2018). However, our results indicate that these approaches ignore the effects of FPD on the coupling between deformations normal and parallel to the fractures which, in turn, can lead to incorrect estimates of the seismic signatures of the probed medium. The complete assessment of the effective anisotropic response of a fluid-saturated porous rock mass with aligned fractures of finite thickness considerably depends on the additional excess compliances that are present in the TLM. Care must be taken when using the LST approach to model this response, as its inherent limitations to account for anisotropic FPD effects could lead to an incorrect characterization of the fractured reservoir of interest.

REFERENCES

Backus, G.E., 1962. Long-wave elastic anisotropy produced by horizontal layering, *J. geophys. Res.,* **67**(11), 4427–4440.

Baird, A.F., Kendall, J.-M. & Angus, D.A., 2013. Frequency-dependent seismic anisotropy due to fractures: fluid flow versus scattering, *Geophysics,* **78**(2), WA111–WA122.

Bakulin, A., Grechka, V. & Tsvankin, I., 2000. Estimation of fracture parameters from reflection seismic data - Part I: HTI model due to a single fracture set, *Geophysics,* **65**(6), 1788–1802.

Barbosa, N.D., Rubino, J.G., Caspari, E. & Holliger, K., 2017. Sensitivity of seismic attenuation and phase velocity to intrinsic background anisotropy in fractured porous rocks: a numerical study, *J. geophys. Res.,* **122**(10), 8181–8199.

Barbosa, N.D., Rubino, J.G., Caspari, E. & Holliger, K., 2018. Impact of fracture clustering on the seismic signatures of porous rocks containing aligned fractures, *Geophysics,* **83**(5), MR295–MR308.

Brajanovski, M., Gurevich, B. & Schoenberg, M., 2005. A model for P-wave attenuation and dispersion in a porous medium permeated by aligned fractures, *Geophys. J. Int.,* **163**(1), 372–384.

Carcione, J.M., Gurevich, B., Santos, J.E. & Picotti, S., 2013. Angular and frequency-dependent wave velocity and attenuation in fractured porous media, *Pure appl. Geophys.,* **170**(11), 1673–1683.

Chapman, M., 2003. Frequency-dependent anisotropy due to meso-scale fractures in the presence of equant porosity, *Geophys. Prospect.,* **51**(5), 369–379.

Chen, H. & Innanen, K.A., 2018. Estimation of fracture weaknesses and integrated attenuation factors from azimuthal variations in seismic amplitudes, *Geophysics,* **83**(6), R711–R723.

Chichinina, T., Sabinin, V. & Ronquillo-Jarillo, G., 2006. QVOA analysis: P-wave attenuation anisotropy for fracture characterization, *Geophysics,* **71**(3), C37–C48.

Foord, G., Verdon, J.P. & Kendall, J.-M., 2015. Seismic characterization of fracture compliance in the field using P- and S-wave sources, *Geophys. J. Int.,* **203**(3), 1726–1737.

Galvin, R.J. & Gurevich, B., 2015. Frequency-dependent anisotropy of porous rocks with aligned fractures, *Geophys. Prospect.,* **63**(1), 141–150.

Gassmann, F., 1951. Über die elastizität poröser medien, *Vierteljahrsschrift der Naturforschenden Gesellschaft in Zurich,* **96**, 1–23.

Gelinsky, S. & Shapiro, S.A., 1997. Poroelastic Backus averaging for anisotropic layered fluid- and gas-saturated sediments, *Geophysics,* **62**(6), 1867–1878.

Gibiansky, L. & Torquato, S., 1998. Rigorous connection between physical properties of porous rocks, *J. geophys. Res.,* **103**(B10), 23 911–23 923.

Guo, J., Rubino, J.G., Barbosa, N.D., Glubokovskikh, S. & Gurevich, B., 2018. Seismic dispersion and attenuation in saturated porous rocks with aligned fractures of finite thickness: Theory and numerical simulations - Part 2: frequency-dependent anisotropy, *Geophysics,* **83**(1), WA49–WA62.

Gurevich, B., 2003. Elastic properties of saturated porous rocks with aligned fractures, *J. appl, Geophys.,* **54**, 203–218.

Kong, L., Gurevich, B., Zhang, Y. & Wang, Y., 2017. Effect of fracture fill on frequency-dependent anisotropy of fractured porous rocks, *Geophys. Prospect.,* **65**(6), 1649–1661.

Krzikalla, F. & Müller, T.M., 2011. Anisotropic P-SV-wave dispersion and attenuation due to inter-layer flow in thinly layered porous rocks, *Geophysics,* **76**(3), WA135–WA145.

Li, J., Li, H., Jiao, Y., Liu, Y., Xia, X. & Yu, C., 2014. Analysis for oblique wave propagation across filled joints based on thin-layer interface model, *J. appl. Geophys.,* **102**, 39–46.

Liu, E., Hudson, J.A. & Pointer, T., 2000. Equivalent medium representation of fractured rock, *J. geophys. Res.,* **105**(B2), 2981–3000.

Maultzsch, S., Chapman, M., Liu, E. & Li, X.Y., 2003. Modelling frequency-dependent seismic anisotropy in fluid-saturated rock with aligned fractures: implication of fracture size estimation from anisotropic measurements, *Geophys. Prospect.,* **51**(5), 381–392.

Mavko, G., Mukerji, T. & Dvorkin, J., 2009. *The Rock Physics Handbook: Tools for Seismic Analysis of Porous Media,* Cambridge Univ. Press.

Müller, T.M., Gurevich, B. & Lebedev, M., 2010. Seismic wave attenuation and dispersion resulting from wave-induced flow in porous rocks - a review, *Geophysics,* **75**, 147–163.

Picket, G., 1963. Acoustic character logs and their application in formation evaluation, *J. Petrol. Technol.,* **15**(06), 659–667.

Pride, S.R., 2005. Relationships between seismic and hydrological properties, in *Hydrogeophysics,* chap.9, pp. 253–290, eds Rubin, Y. & Hubbard, S., Springer.

Pyrak-Nolte, L.J., Myer, L.R. & Cook, N. G.W., 1990. Transmission of seismic waves across single natural fractures, *J. geophys. Res.,* **95**(B6), 8617–8638.

Rubino, J.G. & Holliger, K., 2012. Seismic attenuation and velocity dispersion in heterogeneous partially saturated porous rocks, *Geophys. J. Int.,* **188**, 1088–1102.

Rubino, J.G., Velis, D.R. & Holliger, K., 2012. Permeability effects on the seismic response of gas reservoirs, *Geophys. J. Int.,* **189**, 448–468.

Rubino, J.G., Müller, T.M., Guarracino, L., Milani, M. & Holliger, K., 2014. Seismoacoustic signatures of fracture connectivity, *J. geophys. Res.,* **119**, 2252–2271.

Rubino, J.G., Castromán, G.A., Müller, T.M., Monachesi, L.B., Zyserman, F.I. & Holliger, K., 2015. Including poroelastic effects in the linear slip theory, *Geophysics,* **80**, A51–A56.

Rubino, J.G., Caspari, E., Müller, T.M., Milani, M., Barbosa, N.D. & Holliger, K., 2016. Numerical upscaling in 2-D heterogeneous poroelastic rocks: anisotropic attenuation and dispersion of seismic waves, *J. geophys. Res.,* **121**(9), 6698–6721.

Schoenberg, M., 1980. Elastic wave behavior across linear slip interfaces, *J. acoust. Soc. Am.,* **68**(5), 1516–1521.

Schoenberg, M. & Douma, J., 1988. Elastic wave propagation in media with parallel fractures and aligned cracks, *Geophys. Prospect.,* **36**(6), 571–590.

Schoenberg, M. & Sayers, C.M., 1995. Seismic anisotropy of fractured rock, *Geophysics,* **60**(1), 204–211.

Thomsen, L., 1986. Weak elastic anisotropy, *Geophysics,* **51**(10), 1954–1966.

Verdon, J.P., Kendall, J.-M. & Wüstefeld, A., 2009. Imaging fractures and sedimentary fabrics using shear wave splitting measurements made on passive seismic data, *Geophys. J. Int.,* **179**(2), 1245–1254.

Vizuett, K. C.A. & Davis, T., 2017. Application of the seismic quality factor versus offset and azimuth (QVOA) for fractured reservoir characterization, *First Break,* **35**(10), 55–60.

White, J.E., Mikhaylova, N.G. & Lyakhovitsky, F.M., 1975. Low-frequency seismic waves in fluid-saturated layered rocks, *Phys. Solid Earth,* **11**, 654–659.

Xue, J., Gu, H. & Cai, C., 2017. Model-based amplitude versus offset and azimuth inversion for estimating fracture parameters and fluid content, *Geophysics,* **82**(2), M1–M17.

APPENDIX: COEFFICIENTS OF THE RELAXED AND UNRELAXED EFFECTIVE STIFFNESS MATRICES

In the unrelaxed case, the coefficients of the effective stiffness matrix $\mathbf{C}^u$ of the layered medium are (Barbosa *et al.* 2018)

$$C_{11}^u = \left\langle \frac{1}{P^{\mathrm{sat}}} \right\rangle^{-1}, \tag{A1}$$

$$C_{12}^u = \left\langle \frac{1}{P^{\text{sat}}} \right\rangle^{-1} \left\langle \frac{\lambda^{\text{sat}}}{P^{\text{sat}}} \right\rangle, \tag{A2}$$

$$C_{13}^u = C_{12}^u, \tag{A3}$$

$$C_{22}^u = \left\langle \frac{4\mu\left(\lambda^{\text{sat}} + \mu\right)}{P^{\text{sat}}} \right\rangle + \left\langle \frac{1}{P^{\text{sat}}} \right\rangle^{-1} \left\langle \frac{\lambda^{\text{sat}}}{P^{\text{sat}}} \right\rangle^2, \tag{A4}$$

$$C_{23}^u = \left\langle \frac{2\mu\lambda}{P^{\text{sat}}} \right\rangle + \left\langle \frac{1}{P^{\text{sat}}} \right\rangle^{-1} \left\langle \frac{\lambda^{\text{sat}}}{P^{\text{sat}}} \right\rangle^2, \tag{A5}$$

$$C_{33}^u = C_{22}^u, \tag{A6}$$

$$C_{44}^u = \langle \mu \rangle, \tag{A7}$$

$$C_{55}^u = \left\langle \frac{1}{\mu} \right\rangle^{-1}, \tag{A8}$$

$$C_{66}^u = C_{55}^u. \tag{A9}$$

Here, $\langle F \rangle$ refers to the thickness-weighted average of the enclosed property F, that is, $\langle F \rangle = h_b F_b + h_c F_c$ with the subscripts b and c referring to background and fracture properties, respectively. In eqs (A1) to (A9), the undrained Lamé parameter λ^{sat} and the undrained P-wave modulus P^{sat} are given by

$$\lambda^{\text{sat}} = K^{\text{dry}} - \frac{2}{3}\mu + \alpha^2 M, \tag{A10}$$

$$P^{\text{sat}} = \lambda^{\text{sat}} + 2\mu. \tag{A11}$$

The Biot–Willis coefficient α and the fluid storage modulus M are given by

$$\alpha = 1 - \frac{K^{\text{dry}}}{K_g}, \tag{A12}$$

$$M = \left(\frac{\alpha - \phi}{K_g} + \frac{\phi}{K_f} \right)^{-1}. \tag{A13}$$

In the relaxed case, the coefficients of the stiffness matrix $\mathbf{C}^r$ are given by (Barbosa *et al.* 2018)

$$C_{11}^r = \left\langle \frac{1}{P^{\text{dry}}} \right\rangle^{-1} + \frac{Y^2}{Z}, \tag{A14}$$

$$C_{12}^r = \left\langle \frac{1}{P^{\text{dry}}} \right\rangle^{-1} \left\langle \frac{\lambda^{\text{dry}}}{P^{\text{dry}}} \right\rangle + \frac{XY}{Z}, \tag{A15}$$

$$C_{13}^r = C_{12}^r, \tag{A16}$$

$$C_{22}^r = \left\langle \frac{4\mu\left(\lambda^{\text{dry}} + \mu\right)}{P^{\text{dry}}} \right\rangle + \left\langle \frac{1}{P^{\text{dry}}} \right\rangle^{-1} \left\langle \frac{\lambda}{P^{\text{dry}}} \right\rangle^2 + \frac{X^2}{Z}, \tag{A17}$$

$$C_{23}^r = \left\langle \frac{2\mu\lambda^{\text{dry}}}{P^{\text{dry}}} \right\rangle + \left\langle \frac{1}{P^{\text{dry}}} \right\rangle^{-1} \left\langle \frac{\lambda}{P^{\text{dry}}} \right\rangle^2 + \frac{X^2}{Z}, \tag{A18}$$

$$C_{33}^r = C_{22}^r, \tag{A19}$$

$$C_{44}^r = \langle \mu \rangle, \tag{A20}$$

$$C_{55}^r = \left\langle \frac{1}{\mu} \right\rangle^{-1}, \tag{A21}$$

$$C_{66}^r = C_{55}^r, \tag{A22}$$

where λ^{dry} and P^{dry} correspond to the dry Lamé parameter and the dry P-wave modulus, respectively

$$\lambda^{\text{dry}} = K^{\text{dry}} - \frac{2}{3}\mu, \tag{A23}$$

$$P^{\text{dry}} = \lambda^{\text{dry}} + 2\mu. \tag{A24}$$

The poroelastic constants X, Y and Z are computed as

$$X = -Z\left(\left\langle\frac{2\alpha\mu}{P^{\text{dry}}}\right\rangle + \left\langle\frac{\alpha}{P^{\text{dry}}}\right\rangle\left\langle\frac{\lambda^{\text{dry}}}{P^{\text{dry}}}\right\rangle\left\langle\frac{1}{P^{\text{dry}}}\right\rangle^{-1}\right),\tag{A25}$$

$$Y = -Z\left\langle\frac{\alpha}{P^{\text{dry}}}\right\rangle\left\langle\frac{1}{P^{\text{dry}}}\right\rangle^{-1},\tag{A26}$$

$$Z = \left(\left\langle\frac{1}{M}\right\rangle + \left\langle\frac{\alpha^2}{P^{\text{dry}}}\right\rangle - \left\langle\frac{\alpha}{P^{\text{dry}}}\right\rangle^2\left\langle\frac{1}{P^{\text{dry}}}\right\rangle^{-1}\right)^{-1}.\tag{A27}$$